Journal of Computational Physics 228 (2009) 8093–8111

Contents lists available at ScienceDirect

Journal of Computational Physics

journal homepage: www.elsevier.com/locate/jcp

Electromagnetic MUSIC-type imaging of perfectly conducting, arc-like cracks at single frequency

Won-Kwang Park, Dominique Lesselier *

Département de Recherche en Électromagnétisme, Laboratoire des Signaux et Systèmes, UMR8506 (CNRS-Supélec-Université Paris-Sud 11), 91192 Gif-sur-Yvette cedex, France

ARTICLE INFO

Article history:
Received 27 April 2009
Received in revised form 24 July 2009
Accepted 27 July 2009
Available online 4 August 2009

Keywords:
Non-iterative imaging
Perfectly conducting cracks
Multi-Static Response (MSR) matrix
MUSIC
Numerical experiments

ABSTRACT

We propose a non-iterative MUSIC (MUltiple SIgnal Classification)-type algorithm for the time-harmonic electromagnetic imaging of one or more perfectly conducting, arc-like cracks found within a homogeneous space $\mathbb{R}^2$. The algorithm is based on a factorization of the Multi-Static Response (MSR) matrix collected in the far-field at a single, nonzero frequency in either Transverse Magnetic (TM) mode (Dirichlet boundary condition) or Transverse Electric (TE) mode (Neumann boundary condition), followed by the calculation of a MUSIC cost functional expected to exhibit peaks along the crack curves each half a wavelength. Numerical experimentation from exact, noiseless and noisy data shows that this is indeed the case and that the proposed algorithm behaves in robust manner, with better results in the TM mode than in the TE mode for which one would have to estimate the normal to the crack to get the most optimal results.

1. Introduction

The time-harmonic inverse scattering from an open, smoothly shaped arc in two-dimensions which is satisfying a Dirichlet boundary condition has been investigated in depth in [18]. In this paper, the integral equation over the arc is first used to prove the existence and uniqueness of the solution and to compute it by developing a rigorous Nyström solution method. Then, the retrieval of the arc itself is carried out via a Newton-type iterative scheme. This approach works as well for a Neumann inverse scattering problem, using the material proposed in [19] on the direct problem in this case, and one then refers to [20].

Yet, for successful application of such solution schemes, a good initial guess is needed, hopefully close enough to the unknown scatterer. Without it, one might suffer from large computational costs, with the risk of non convergence also. Moreover, such iterative schemes require calculation of the Fréchet derivative of the far-field operator and call for regularization terms that are expected to depend on the specific problem at hand, and whose proper choice involves a good degree of numerical experimentation.

In the present contribution, we choose to focus onto an imaging algorithm which provides in one single step and with the least amount of calculation the shape of a perfectly conducting crack (arc-like) from the scattered far-field patterns observed when a finite number of time-harmonic, single-frequency plane waves are impinging upon it. Let us emphasize that, even though the shape which the present algorithm yields does not guarantee us a full retrieval of the crack, this limitation being in accord with the Rayleigh criterion, it might provide at least a good initial guess of further, more elaborate iterative procedures of imaging.

* Corresponding author. Tel.: +33 169851561; fax: +33 169851765.
E-mail address: lesselier@lss.supelec.fr (D. Lesselier).

0021-9991/$ - see front matter © 2009 Elsevier Inc. All rights reserved.
doi:10.1016/j.jcp.2009.07.026

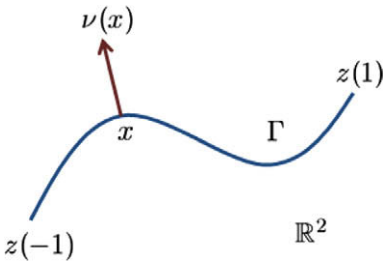

Fig. 1. Illustration of a two-dimensional arc-like crack Γ.

The analysis is led in a two-dimensional setting in both standard electromagnetic polarization cases, the Transverse Magnetic (TM) one for which a Dirichlet boundary condition is holding on the crack, and the Transverse Electric (TE) for which a Neumann boundary condition is holding on it, being emphasized that the imaging algorithm works as well for multiple, non-intersecting cracks, and in fluid acoustics.[1] In effect, the algorithm is simply based on a factorization of the far-field Multi-Static Response (MSR) matrix (deduced from the far-field patterns) followed by the calculation of a MUSIC cost functional the map of which is expected to exhibit a finite number of peaks along the crack, one each half a wavelength in view of the standard resolution limit.

The paper itself is organized as follows. In Section 2, the direct scattering problem is introduced and the far-field pattern of the scattered field is described in some detail, here mostly for the sake of completeness since this material is classical nowadays. In Section 3, where most novelty lies in, the factorization of the MSR matrix is carried out, interpreted, and the MUSIC-type imaging algorithm which it enables us to derive is discussed briefly for both boundary conditions/polarizations. In Sections 4 and 5, a set of numerical results is proposed, such as spectra of MSR matrices, and images of one and two cracks, from noiseless and noisy, discrete TM and TE data, such data being computed in rigorous fashion from the application of the Nyström method or by alternative methods. A short conclusion follows.

A brief description of the present work can be found in the forthcoming conference paper [25]. Much more, as well as other investigations of the retrieval of arc-like cracks in static and propagative regimes is in the thesis of the first author [22]. Otherwise, let us refer to [8,9,11,17,18] as useful references that investigate the so-called linear sampling method, as another imaging algorithm linked to the MUSIC one, being mentioned that a Tikhonov regularization appears to be required for any successful reconstruction. The relationship between the MUSIC and the linear sampling method is studied in [10]. No attempt is made here to review that existing or potential linkage, whilst such references are acknowledged not to be exhaustive on the issue of linear sampling.

2. Helmholtz equation and direct scattering problem

Let $\Gamma \subset \mathbb{R}^2$ be an oriented, piecewise smooth, non self-intersecting arc without cusp which describes the crack, i.e.,

$$\Gamma = \{z(s) : s \in [-1,1]\},$$

where $z : [-1,1] \to \mathbb{R}^2$ is an injective piecewise C^3 function (see sketch in Fig. 1), and let us henceforth assume that the said crack is perfectly conducting.

First, let us consider the so-called Transverse Magnetic polarization case, letting u be the (single-component) electric field that satisfies the two-dimensional Helmholtz wave equation

$$\Delta u(x) + k^2 u(x) = 0 \quad \text{in } \mathbb{R}^2 \setminus \Gamma, \tag{1}$$

with strictly positive wave number $k = \omega\sqrt{\mu\varepsilon}$, letting ε be the electric permittivity and μ the magnetic permeability. The field cannot penetrate into Γ, i.e., u satisfies the Dirichlet boundary condition

$$u(x) = 0 \quad \text{on } \Gamma. \tag{2}$$

Conversely, let us consider the Transverse Electric polarization case, letting u be the (single-component) magnetic field that satisfies the two-dimensional Helmholtz wave Eq. (1) yet now with the following Neumann boundary condition on Γ:

$$\frac{\partial u}{\partial \nu}(x) = 0 \quad \text{on } \Gamma \setminus \{z(-1), z(1)\}, \tag{3}$$

where $\nu(x)$ is a unit normal vector to Γ at x.

Let us notice that the total field can always be decomposed as $u(x) = u_0(x) + u_s(x), u_0(x) = e^{ik\theta\cdot x}$ the given incident field for incident direction $\theta \in S^1$, and $u_s(x)$ the unknown scattered field, which is required to satisfy the Sommerfeld radiation condition

[1] This would correspond as well to a sound-soft or to a sound-hard screen in a fluid-like medium insonified by compressional waves.

$$\lim_{|x|\to\infty}\sqrt{|x|}\left(\frac{\partial u_s(x)}{\partial|x|}-iku_s(x)\right)=0,$$

uniformly into all directions $\hat{x}=\frac{x}{|x|}$. The determination of u_s is but a special case of the following problem

$$\Delta u_s(x)+k^2u_s(x)=0 \quad \text{in } \mathbb{R}^2\setminus\Gamma, \tag{4}$$

that satisfies the Dirichlet boundary condition

$$u_s(x)=f(x) \quad \text{on } \Gamma, \tag{5}$$

or the Neumann boundary condition

$$\frac{\partial u_s}{\partial\nu}(x)=f(x) \quad \text{on } \Gamma, \tag{6}$$

and the Sommerfeld radiation condition. Let us remind that from the boundary conditions (2) and (3), we can set $f(x)=-u_0(x)$ and $f(x)=-\frac{\partial u_0}{\partial\nu}(x)$ for the boundary conditions (5) and (6), respectively. Let us notice at this stage that the above works only for 'smooth' arcs, and we should refer to [21] for a broader and thoughtful coverage of electromagnetic scattering by general arcs, including ours.

2.1. Existence and uniqueness of the solution

Let us first consider the case of the Dirichlet boundary problem (TM polarization). The author in [18] establishes the existence of a solution by searching it in the form of a single-layer potential

$$u_s(x)=\int_\Gamma \Phi(x,y)\varphi(y;\theta)dy \quad \text{for } x\in\mathbb{R}^2\setminus\Gamma, \tag{7}$$

with the two-dimensional fundamental solution to the Helmholtz equation

$$\Phi(x,y)=\frac{i}{4}H_0^1(k|x-y|) \quad \text{for } x\neq y,$$

expressed in terms of the Hankel function H_0^1 of order zero and of the first kind. The unknown density φ is assumed to be of the form

$$\varphi(x;\theta)=\frac{\widetilde{\varphi}(x;\theta)}{\sqrt{|x-z(-1)||x-z(1)|}} \quad \text{for } x\in\Gamma\setminus\{z(-1),z(1)\}.$$

Here, $\widetilde{\varphi}$ is a continuous function on Γ and $z(-1)$ and $z(1)$ are end-points of Γ. Then, for $1<p<2$, $\varphi\in L^p(\Gamma)$ and therefore, the single-layer potential (7) is continuous throughout $\mathbb{R}^2$. Hence, if the density φ is a solution to the integral equation

$$\int_\Gamma \Phi(x,y)\varphi(y;\theta)dy=f(x) \quad \text{for } x\in\Gamma, \tag{8}$$

then the potential u_s of (7) solves the exterior Dirichlet problem. From [18, Theorem 2.5], the author shows that, if $0<\alpha<1$, for boundary condition $f\in C^{1,\alpha}(\Gamma)$ in (5), the Dirichlet problem for the exterior of an arc has a unique solution and this solution depends continuously on the boundary data.

For the Neumann boundary problem, the author in [19] establishes the existence of a solution by searching it as a double-layer potential

$$u_s(x)=\int_\Gamma \frac{\partial\Phi}{\partial\nu}(x,y)\psi(y;\theta)dy \quad \text{for } x\in\mathbb{R}^2\setminus\Gamma. \tag{9}$$

For $0<\alpha<1$, the unknown density ψ is contained within a space of locally Hölder continuously differentiable functions on Γ which is

$$C^{1,\alpha}_{\mathrm{loc}}(\Gamma\setminus\{z(-1),z(1)\})=\left\{\psi\in C(\Gamma):\psi(z(-1);\theta)=\psi(z(1);\theta)=0,\psi'\in L^1(\Gamma)\right\},$$

where the prime indicates differentiation with respect to the arc length. By using the jump relations for the double-layer potentials, if the density ψ is a solution to the hypersingular integral equation of the first kind

$$\frac{\partial}{\partial\nu}\int_\Gamma \frac{\partial\Phi}{\partial\nu}(x,y)\psi(y;\theta)dy=f(x) \quad \text{for } x\in\Gamma\setminus\{z(-1),z(1)\}, \tag{10}$$

then the potential u_s of (9) solves the exterior Neumann problem. Denoting $\tau(x)$ as tangent vector to $\Gamma\setminus\{z(-1),z(1)\}$ at x, (10) becomes Maue's identity

$$f(x)=\frac{\partial}{\partial\nu}\int_\Gamma \frac{\partial\Phi}{\partial\nu}(x,y)\psi(y;\theta)dy=\int_\Gamma \frac{\partial\Phi}{\partial\tau}(x,y)\frac{\partial\psi}{\partial\tau}(y;\theta)dy+k^2\int_\Gamma \Phi(x,y)\psi(y;\theta)\nu(x)\cdot\nu(y)dy,$$

for $x \in \Gamma \setminus \{z(-1), z(1)\}$. Let us note that, from the above identity, the degree of singularity in the hypersingular integral Eq. (10) has been reduced. In [19, Theorem 2.3], the author shows that the Neumann problem for the exterior of an arc has a unique solution.

2.2. The far-field pattern

Now, we easily derive an integral representation of the far-field pattern of the scattered field u_s. Since, for densities φ, the first derivatives of the total field u can be extended as a continuous function from $\mathbb{R}^2 \setminus \Gamma$ to $\mathbb{R}^2 \setminus \{z(-1), z(1)\}$ with different limiting values on both sides of Γ by using the jump relations for the single-layer potentials. In particular, if we denote $\nu(x)$ as a normal vector to Γ at x, the limits of the following quantities exist

$$
\begin{aligned}
& u(x) = \lim_{h \to +0} u(x \pm h\nu(x)) \\
& \frac{\partial u_\pm}{\partial \nu}(x) = \lim_{h \to +0} \nu(x) \cdot \nabla u(x \pm h\nu(x)) \\
& -\varphi(x;\theta) = \frac{\partial u_+}{\partial \nu}(x) - \frac{\partial u_-}{\partial \nu}(x) \\
& -\psi(x;\theta) = u_+(x) - u_-(x),
\end{aligned}
$$

for all $x \in \Gamma \setminus \{z(-1), z(1)\}$.

So, for every incident field u_0, the total field u that satisfies a Dirichlet boundary condition has the integral representation

$$
u(x) = u_0(x) + u_s(x) = u_0(x) + \int_\Gamma \Phi(x,y)\varphi(y;\theta)dy = u_0(x) - \int_\Gamma \left\{ \frac{\partial u_+}{\partial \nu}(y) - \frac{\partial u_-}{\partial \nu}(y) \right\} \Phi(x,y)dy,
$$

for $x \in \mathbb{R}^2 \setminus \Gamma$.

The far-field pattern u_∞ of the scattered field u_s is defined on the two-dimensional unit circle S^1. It can be represented as

$$
u_s(x) = \frac{e^{ik|x|}}{\sqrt{|x|}} \left\{ u_\infty(\hat{x};\theta) + O\left(\frac{1}{|x|}\right) \right\},
$$

uniformly in all directions $\hat{x} = \frac{x}{|x|}$ and $|x| \to \infty$. From the above representation and the asymptotic formula for the Hankel function [12], we conclude that the far-field pattern for the scattering of an incident field u_0 from a perfectly conducting crack Γ is given by

$$
\begin{aligned}
u_\infty(\hat{x};\theta) &= -\frac{e^{i\frac{\pi}{4}}}{\sqrt{8\pi k}} \int_\Gamma e^{-ik\hat{x}\cdot y} \left\{ \frac{\partial u_+}{\partial \nu}(y) - \frac{\partial u_-}{\partial \nu}(y) \right\} dy, \quad \hat{x} \in S^1 \\
&= \frac{e^{i\frac{\pi}{4}}}{\sqrt{8\pi k}} \int_\Gamma e^{-ik\hat{x}\cdot y} \varphi(y;\theta) dy,
\end{aligned} \tag{11}
$$

for $\hat{x} \in S^1$.

Similarly, the far-field pattern for the Neumann boundary problem can be derived as

$$
\begin{aligned}
u_\infty(\hat{x};\theta) &= \sqrt{\frac{k}{8\pi}} e^{-i\frac{\pi}{4}} \int_\Gamma \hat{x} \cdot \nu(y) e^{-ik\hat{x}\cdot y} \{u_+(y) - u_-(y)\} dy \\
&= \sqrt{\frac{k}{8\pi}} e^{-i\frac{\pi}{4}} \int_\Gamma \hat{x} \cdot \nu(y) e^{-ik\hat{x}\cdot y} \psi(y;\theta) dy,
\end{aligned} \tag{12}
$$

for $\hat{x} \in S^1$.

3. MUSIC-type algorithm for imaging of cracks

In this section, we apply the far-field pattern formulas (11) and (12) to build up a MUSIC-type algorithm for non-iterative imaging of cracks, refer to [14,15,23] for instance.

First, let us consider the Dirichlet boundary condition case. If we exclude the constant $\frac{e^{i\frac{\pi}{4}}}{\sqrt{8\pi k}}$ from formula (11), the MSR matrix K can be written as

$$
K = \int_\Gamma E_D(y) F_D(y)^T dy, \tag{13}
$$

where $E_D(y)$ is the illumination vector

$$
E_D(y) = \left(e^{-ik\hat{x}_1\cdot y}, e^{-ik\hat{x}_2\cdot y}, \ldots, e^{-ik\hat{x}_N\cdot y} \right)^T \Big|_{\hat{x}_j = -\theta_j} = \left(e^{ik\theta_1\cdot y}, e^{ik\theta_2\cdot y}, \ldots, e^{ik\theta_N\cdot y} \right)^T, \tag{14}
$$

and where $F_D(y)$ is the resulting density vector

$$
F_D(y) = (\varphi(y;\theta_1), \varphi(y;\theta_2), \ldots, \varphi(y;\theta_N))^T. \tag{15}
$$

Here, $\{\hat{x}_j\}_{j=1}^N \subset S^1$ is a discrete finite set of observation directions and $\{\theta_l\}_{l=1}^N \subset S^1$ is the same number of incident directions.

Formula (13) is a factorization of the MSR matrix that separates the known incoming plane wave information from the unknown information. The range of K is determined by the span of the E_D corresponding to the Γ, i.e., we can define a signal subspace by using a set of left singular vectors of K (see [14, Section 3]).

Second, let us consider the Neumann boundary condition case. Likewise eliminating the constant $\sqrt{\frac{k}{8\pi}}e^{-i\frac{\pi}{4}}$ from formula (12), the MSR matrix K reads as

$$K = \int_\Gamma E_N(y) F_N(y)^T dy, \tag{16}$$

where $E_N(y)$ is the illumination vector

$$\begin{aligned} E_N(y) &= -\left(\hat{x}_1 \cdot v(y) e^{-ik\hat{x}_1 \cdot y}, \hat{x}_2 \cdot v(y) e^{-ik\hat{x}_2 \cdot y}, \ldots, \hat{x}_N \cdot v(y) e^{-ik\hat{x}_N \cdot y}\right)^T|_{\hat{x}_j = -\theta_j} \\ &= \left(\theta_1 \cdot v(y) e^{ik\theta_1 \cdot y}, \theta_2 \cdot v(y) e^{ik\theta_2 \cdot y}, \ldots, \theta_N \cdot v(y) e^{ik\theta_N \cdot y}\right)^T, \end{aligned} \tag{17}$$

and where $F_N(y)$ is the corresponding density vector

$$F_N(y) = (\psi(y;\theta_1), \psi(y;\theta_2), \ldots, \psi(y;\theta_N))^T. \tag{18}$$

Formula (16) is a factorization of the MSR matrix that, like with the Dirichlet boundary condition case, separates the known incoming plane wave information from the unknown information. The range of K is determined by the span of the E_N corresponding to the Γ, i.e., we can define a signal subspace by using a set of left singular vectors of K.

Let us assume that the crack is divided into M different segments of size of order half the wavelength $\frac{\lambda}{2}$. Having in mind the Rayleigh resolution limit from far-field data, any detail less than one-half of the wavelength cannot be seen, and only one point at each segment is expected to contribute at the image space of the response matrix K (see [2,3,7] for instance). Each of these points, say x_j for $j = 1, 2, \ldots, M$, can in principle be imaged through the standard MUSIC-type imaging. The resolution of the image provided by this technique is of the order of the half-wavelength.

First, let us consider the imaging algorithm for the Dirichlet boundary condition. Let the singular value decomposition of the matrix K be $K = V S \overline{W}^T$, where $V, W \in \mathbb{C}^{N\times N}$ are unitary matrices and where S is a real nonnegative diagonal matrix with components $\lambda_1, \lambda_2, \ldots, \lambda_N$ which satisfies

$$\lambda_1 \geqslant \lambda_2 \geqslant \cdots \geqslant \lambda_M > 0 \quad \text{and } \lambda_j = 0 \quad \text{for } j = M+1, M+2 \ldots, N.$$

Alternatively, λ_j, for $j = M+1, M+2, \ldots, N$, could merely be very small, below the noise level of the system represented by K. Then, the first M columns of the matrix $V, \{v_1, v_2, \ldots, v_M\}$, provide an orthonormal basis for K and the rest of the matrix $V, \{v_{M+1}, v_{M+2}, \ldots, v_N\}$, provides a basis for the null (or noise) space of K. So, one can form the projection onto the null (or noise) subspace: this projection is given explicitly by

$$P_{\text{noise}}(f) = \sum_{j>M} v_j \overline{v}_j^T f. \tag{19}$$

For any point $x \in \mathbb{R}^2$, let us define a vector $g(x) \in \mathbb{C}^N$ as

$$g(x) = \left(e^{ik\theta_1 \cdot x}, e^{ik\theta_2 \cdot x}, \ldots, e^{ik\theta_N \cdot x}\right)^T. \tag{20}$$

Then there exists $n_0 \in \mathbb{N}$ such that for any $N \geqslant n_0$, the following statement holds [4–6,16]:

$$g(x) \in \text{Range}(K) \quad \text{if and only if } x \in \{x_1, x_2, \ldots, x_M\}.$$

It means that if a point x satisfies $x \in \{x_1, x_2, \ldots, x_M\}$ then $\|P_{\text{noise}}(g(x))\| = 0$. Thus an image of $x_j, j = 1, 2, \ldots, M$, follows from computing

$$W(x) = \frac{1}{\|P_{\text{noise}}(g(x))\|}. \tag{21}$$

The resulting plot of this estimator is expected to exhibit peaks of high magnitude at the sought $x_j \in \Gamma$.

The imaging algorithm for the Neumann boundary condition case is very similar to the previous one (see [14, Section 4] also). For any point $x \in \mathbb{R}^2$, we define a vector $g(x) \in \mathbb{C}^N$ that reads, instead of (20), as

$$g(x) = \left(\theta_1 \cdot v(x) e^{ik\theta_1 \cdot x}, \theta_2 \cdot v(x) e^{ik\theta_2 \cdot x}, \ldots, \theta_N \cdot v(x) e^{ik\theta_N \cdot x}\right)^T. \tag{22}$$

Since the unit normal $v(x)$ is still unknown, for each point x of the search domain, we use a set of directions v_l for $l = 1, 2, \ldots, L$ and we choose $v_l(x)$ which is to maximize

$$W(x) = \frac{1}{\|P_{\text{noise}}(g(x))\|}. \tag{23}$$

The resulting plot of this estimator is again expected to exhibit high peaks at the sought $x_j \in \Gamma$.

4. Numerical examples: Dirichlet boundary condition – TM

In this section, we present some numerical examples obtained with the MUSIC-type algorithms for imaging arc-like cracks satisfying the Dirichlet boundary condition (TM polarization). Throughout this section, the applied wave number is taken of the form $k = \frac{2\pi}{\lambda}$; here λ is the given wavelength, which will be varied between a low-frequency one of $\lambda = 1$ and a high-frequency one of $\lambda = 0.1$.

Three Γ_j are chosen for illustration:

$$\Gamma_1 = \left\{\left(\tfrac{s}{2}, 0.3\right) : s \in [-1,1]\right\},$$
$$\Gamma_2 = \left\{\left(s, \tfrac{1}{2}\cos\tfrac{s\pi}{2} + \tfrac{1}{5}\sin\tfrac{s\pi}{2} - \tfrac{1}{10}\cos\tfrac{3s\pi}{2}\right) : s \in [-1,1]\right\},$$
$$\Gamma_3 = \left\{\left(2\sin\tfrac{s}{2}, \sin s\right) : s \in \left[\tfrac{\pi}{4}, \tfrac{7\pi}{4}\right]\right\},$$

and the search domain Ω is taken as $\Omega = [-1,1]\times[-1,1]$ for the imaging of Γ_1 and Γ_2 and $[-1,3]\times[-2,2]$ for the one of Γ_3. For each $z \in \Omega$, the step size of z is taken of the order of 0.02. As for the observation directions θ_l, they are taken as

$$\theta_l = \left(\cos\frac{2\pi l}{N}, \sin\frac{2\pi l}{N}\right) \quad \text{for } l = 1,2,\ldots,N. \tag{24}$$

It is worth mentioning that, since the reliable and efficient solution of the direct scattering problem indicated previously is very important, all numerical data in this section (the elements $u_\infty(\theta_j,\theta_l)$ for $j,l = 1,2,\ldots,N$ of the dataset K) are generated by the Nyström method for both the Dirichlet and Neumann boundary conditions as presented in [18, formula (4.11)] and [19, p. 354], respectively. After obtaining the dataset, the singular value decomposition of $K = V S \overline{W}^T$ is performed. Unfortunately, in contrast with the theoretical analysis, the computed singular values do not separate neatly between non-zero and zero sets, refer to bottom row of Fig. 2 (see [14, Figure 2] for an extended target case). This phenomenon is also in contrast with most results on the distribution of singular values presented in [4]. So, a careful thresholding is required to discriminate

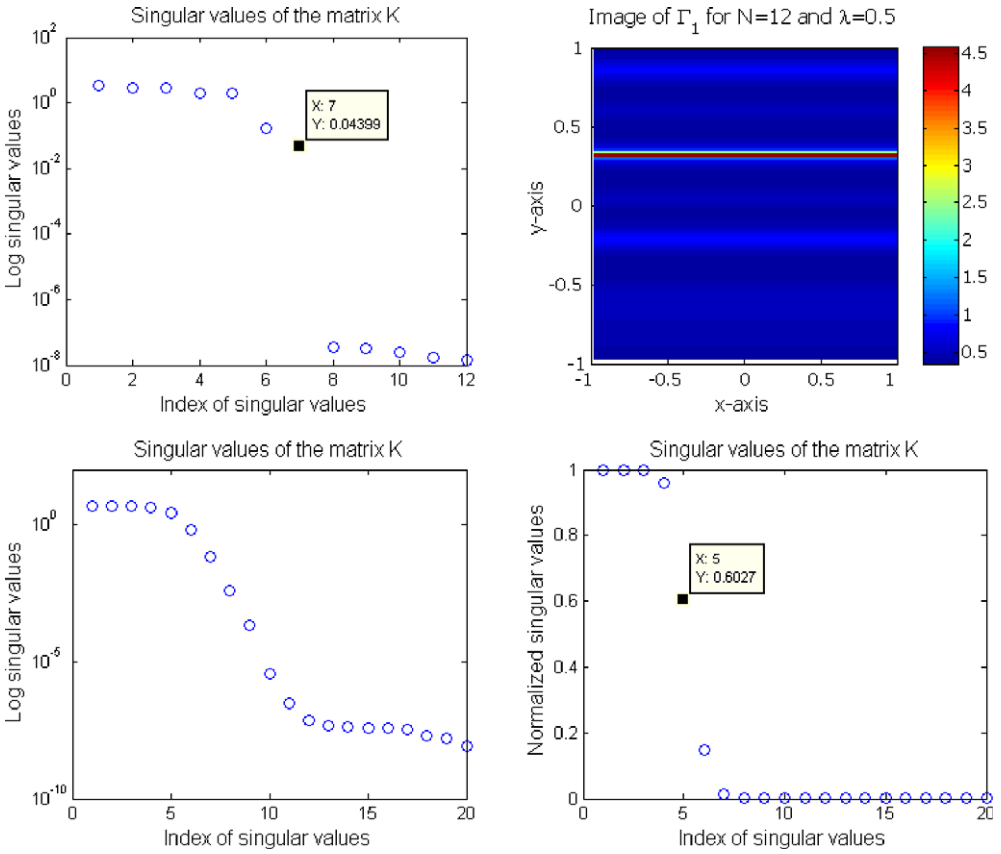

Fig. 2. (Dirichlet boundary condition) Top: Distribution of log-scaled singular values of the matrix K (left) and map of $W(x)$ (right), for $N = 12$ incidences and a 0.5 wavelength. Bottom: Distribution of log-scaled (left) and normalized (right) singular values of the matrix K respectively for $N = 20$ incidences and a 0.5 wave length when the crack is Γ_1.

the singular values that are significant of the signal subspace (and vectors spanning it) from those that are associated to the noise subspace (and vectors spanning it). Once the singular values are computed, they are normalized with respect to the one of maximum amplitude. A detailed discussion of this normalization has been made in [23, Section 4] and every distribution of normalized singular values can be found in [22, Chapter 4].

4.1. Reconstruction of a single crack

Before starting this section, we make the following remarks.

Remark 4.1. Let us consider an image of Γ_1. In Fig. 2, we observe that when the number N is not large enough, we can choose the nonzero singular values without normalizing them, but the imaging is poor. For example, with $N = 12$ and $\lambda = 0.5$, we observe that the first seven singular values are well distinguished from the five, much weaker remaining ones (top left) without normalizing the singular values. However, when we use seven singular values to discriminate the noise subspace from the signal subspace, poor results appear (top right). When we increase N to 20 while keeping the same 0.5 wavelength, this phenomenon disappears (bottom left). Hence, to get a suitable image, one has to take a large enough N and normalize the singular values as well.

Remark 4.2. Instead of the scattered field dataset generated from the Nyström method, some authors introduce a similar formulation involving the solution of a second-kind Fredholm integral equation along the crack, refer to [21, Chapter 3]. Numerical experimentation shows that images of a crack from data acquired by the Nyström method or from the ones calculated via this alternative formulation are almost indistinguishable (see Fig. 3).

Let us first work with Γ_1, K being collected for $N = 20$ and $N = 32$, and wavelengths $\lambda = 0.4$ and $\lambda = 0.2$, respectively. Distributions of the normalized singular values of K and maps of $W(x)$ are displayed in Fig. 4.

Each time, a small finite number of singular values (6 at $\lambda = 0.4, 11$ at $\lambda = 0.2$) emerges from the remaining, much smaller ones, whilst images thereupon produced by projection onto singular vectors beyond the first 6 or 11 ones

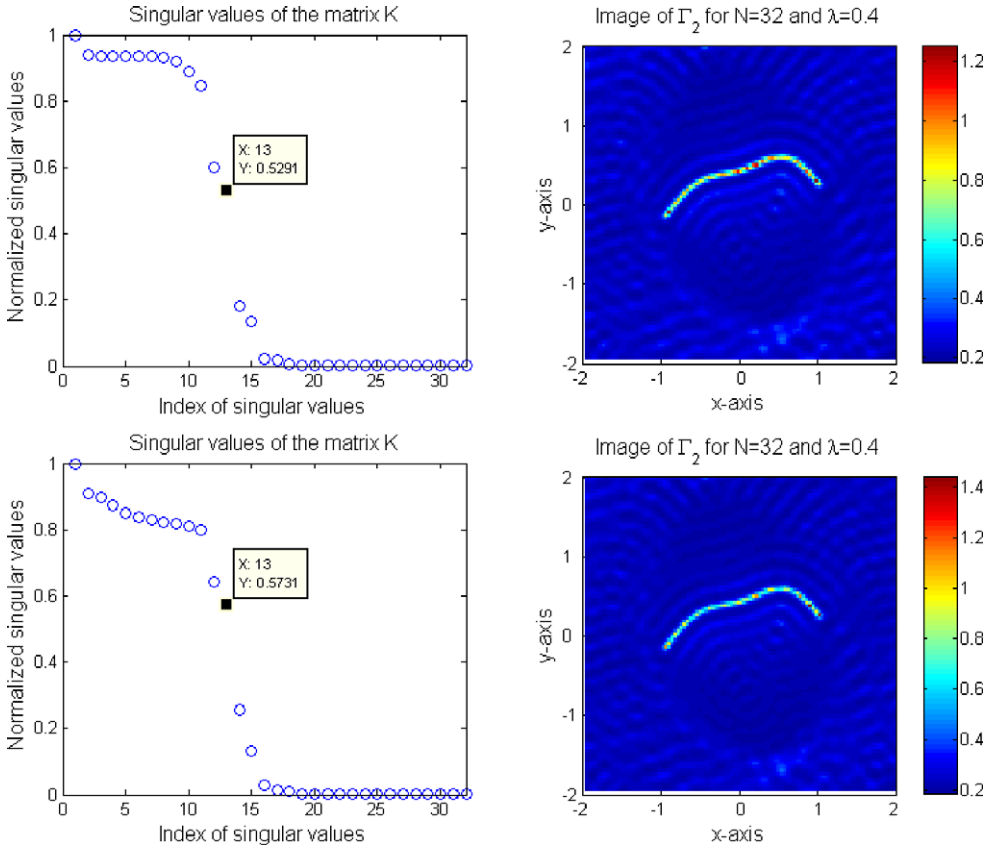

Fig. 3. (Dirichlet boundary condition) Distribution of normalized singular values of the MSR matrix K (left column) and maps of $W(x)$ (right column), for $N = 32$ incidences and a $\lambda = 0.4$ wavelength when the crack is Γ_2. Dataset generated by the Nyström method introduced in [18] (top row) and another one in [21] (bottom row).

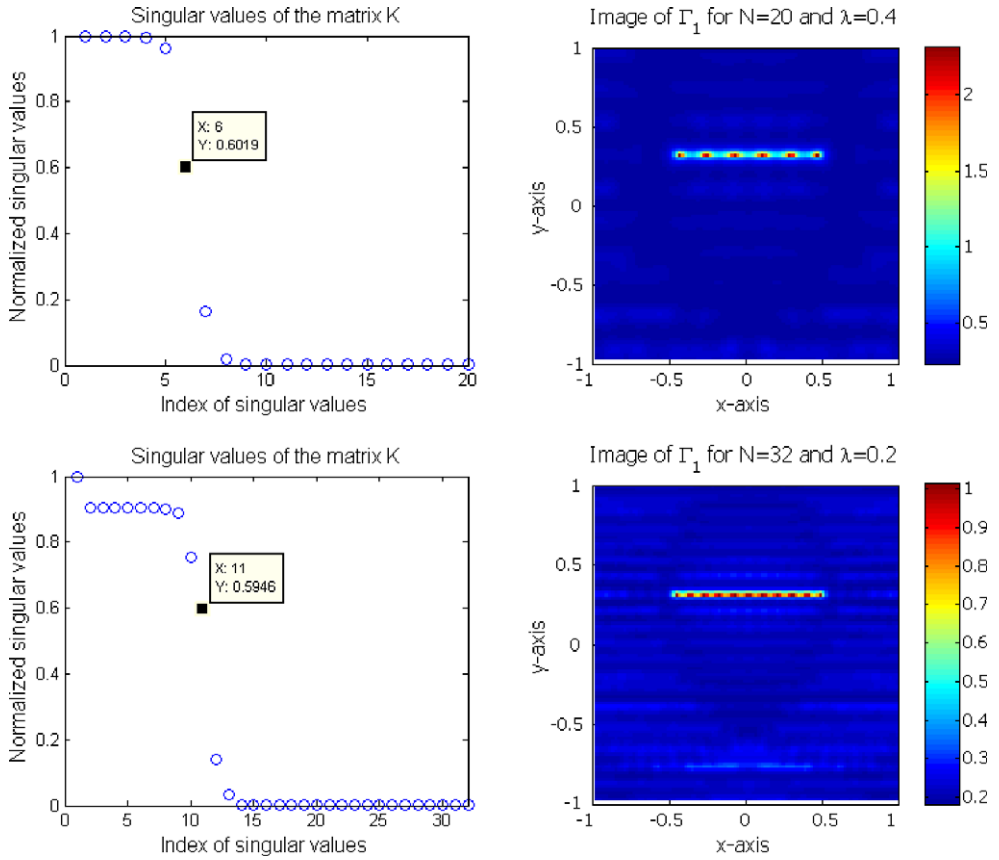

Fig. 4. (Dirichlet boundary condition) Distributions of normalized singular values of the matrix K (left column) and maps of $W(x)$ (right column), for $N = 20$ incidences and a 0.4 wavelength (top row), for $N = 32$ incidences and a 0.2 wavelength (bottom row) when the crack is Γ_1.

appear excellent, a small number of peaks being obtained, each peak being observed to be $\lambda/2$ away from the next one. No problem of discrimination is faced, and this in effect remains true whenever a curve of zero curvature is to be imaged, whatever be its type of contrast and the conditions of illumination (if the ratio N/M is kept properly large).

Opposite to the penetrable inclusion case as dealt with in [23], although the crack is not anymore a straight line, the discrimination for a curved crack is still obvious. As an example, let us consider the image of Γ_2, here using $N = 16$ and $N = 64$ incident directions and a wavelength of 0.8 and 0.2 respectively, refer to Fig. 5.

In addition, the discrimination for a complicated crack, though remaining patent, is affected by unexpected isolated peaks of large magnitude. An image of Γ_3, here using $N = 32$ incident directions and a wavelength $\lambda = 0.7$, shows that phenomenon in Fig. 6.

We have already examined and discussed a similar case from [23]. However, when we increase the number of illuminations to $N = 48$, these peaks do not disappear from the image. Hence, to eliminate them, we have to adopt a much smaller threshold of 0.1 or 0.01, refer to Fig. 7. Comparing with Fig. 6, we observe that this eliminates all or almost all isolated peaks from the images and offers a higher resolution overall.

Now, we apply the algorithm to an oscillating crack. The configuration is the same as previously save the search domain $\Omega = [-1.5, 1.5] \times [-1.5, 1.5]$. Two Γ_j are chosen for illustration (see Fig. 8):

$$\Gamma_4 = \{(s, 0.5s^2 + 0.1\sin(4\pi(s+1)) : s \in [-1,1]\},$$
$$\Gamma_5 = \{(s, 0.5s^2 + 0.05\sin(20\pi(s+1)) - 0.01\cos(15\pi s) : s \in [-1,1]\}.$$

Let us consider Γ_4. Imaging results are displayed in Fig. 9 at $\lambda = 0.6$ and $\lambda = 0.2$. The imaging is rather coarse at the low wavelength, better at the high one. The threshold looks convenient, whilst a high value of N is to be taken as expected.

For the case of a more oscillating crack Γ_5, the results are coarse, as is seen in Fig. 10, but they can be considered as an initial guess close to the true one of a Newton-type iteration method in line with [18].

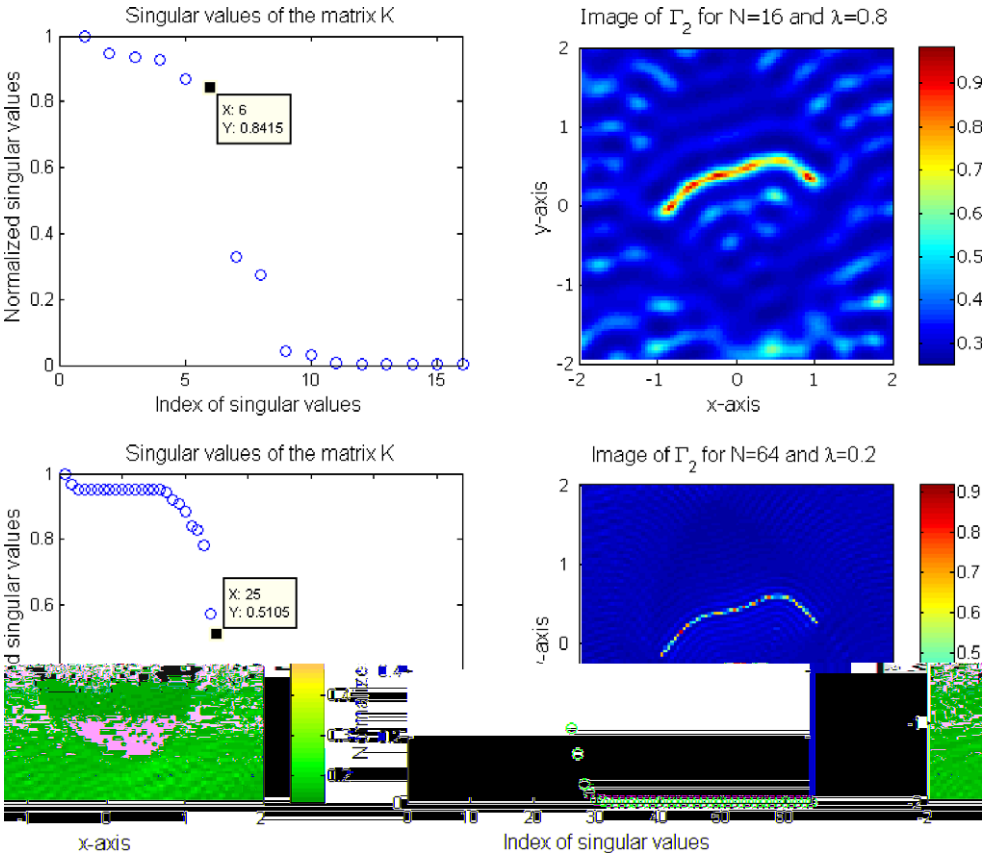

Fig. 5. (Dirichlet boundary condition) Distributions of normalized singular values of the matrix K (left column) and maps of $W(x)$ (right column), for $N = 16$ incidences and a 0.8 wavelength (top row), for $N = 64$ incidences and a 0.2 wavelength (bottom row) when the crack is Γ_2.

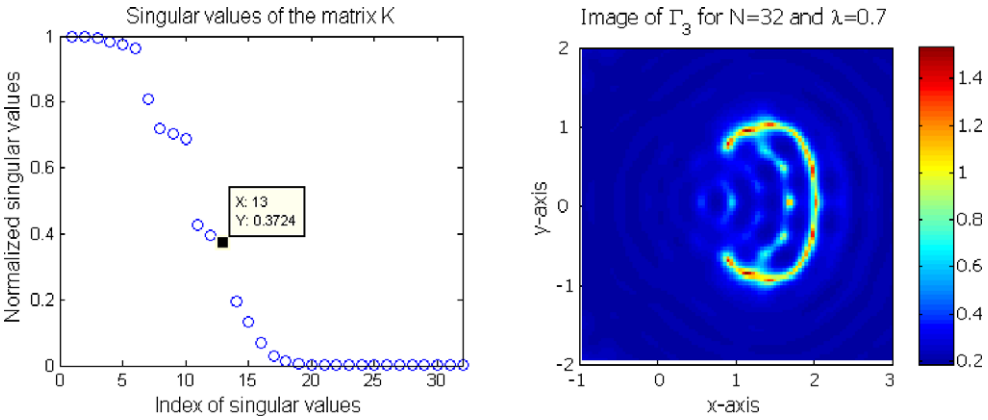

Fig. 6. (Dirichlet boundary condition) Distribution of normalized singular values of the matrix K (left) and map of $W(x)$ (right), for $N = 32$ incidences and a 0.7 wavelength when the crack is Γ_3.

4.2. Extension to multiple cracks

Both the mathematical configuration and the numerical analysis could be extended in somewhat straightforward fashion to the case of multiple inclusions. We will not present the derivation herein and simply provide examples of imaging via the MUSIC-type algorithm in several figures.

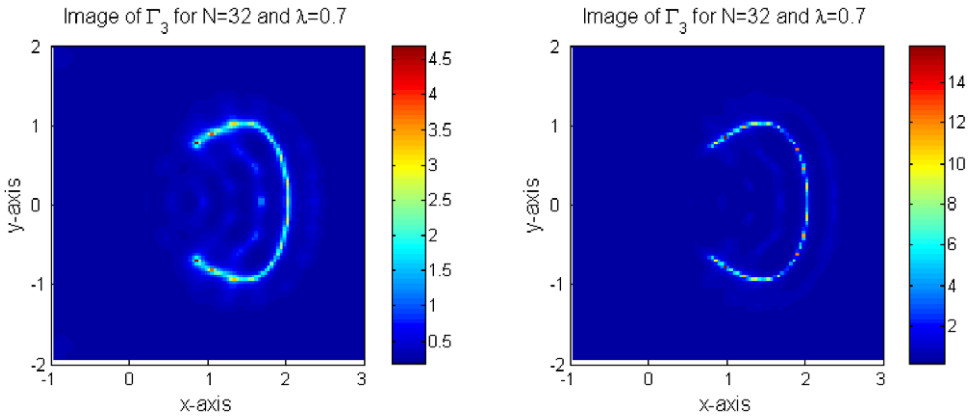

Fig. 7. Same as Fig. 6 except that one has adopted a 0.1 threshold (left) and a 0.01 threshold (right).

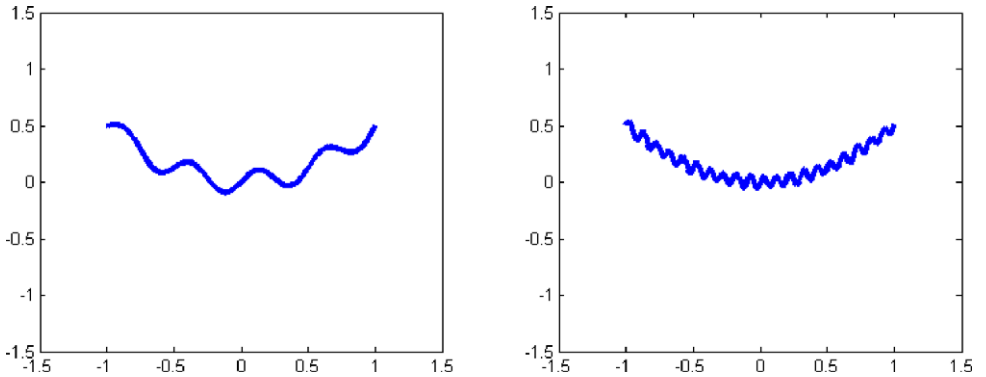

Fig. 8. Shape of Γ_4 (left) and Γ_5 (right).

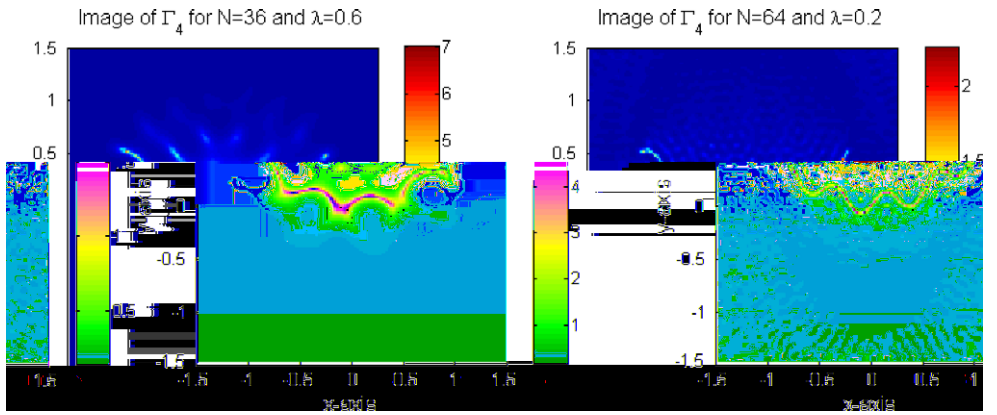

Fig. 9. (Dirichlet boundary condition) Maps of $W(x)$ (right column), for $N = 36$ incidences and $\lambda = 0.6$ wavelength (left) and for $N = 64$ and $\lambda = 0.2$ (right), when the crack is Γ_4.

Let us notice that the elements $u_\infty(\theta_j, \theta_l)$ for $j, l = 1, 2, \ldots, N$ of dataset K are generated from the Nyström method now applied to scattering by more than one crack.

Let us consider the following cracks

$$\Gamma_a = \sigma_1 \cup \sigma_2,$$
$$\Gamma_b = \sigma_3 \cup \sigma_4,$$

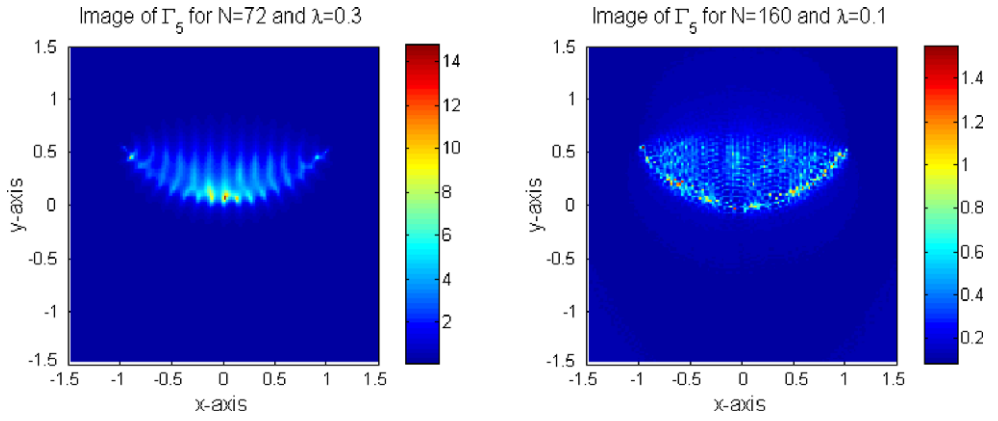

Fig. 10. (Dirichlet boundary condition) Maps of $W(x)$ for $N = 72$ incidences and a 0.3 wavelength (left) and for $N = 160$ incidences and a 0.1 wavelength (right) when the crack is Γ_5.

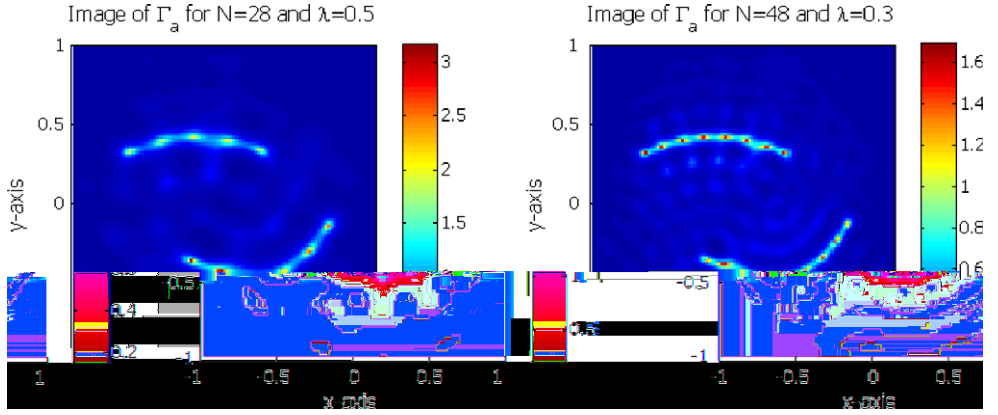

Fig. 11. (Dirichlet boundary condition) Maps of $W(x)$ for $N = 28$ incidences and a 0.5 wavelength (left), for $N = 48$ incidences and a 0.3 wavelength (right) when the crack is Γ_a.

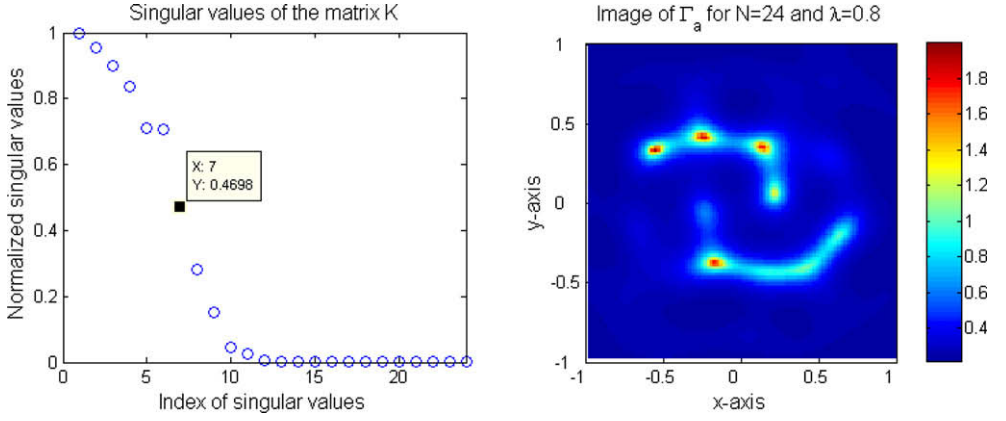

Fig. 12. (Dirichlet boundary condition) Distribution of normalized singular values of the MSR matrix K (left) and map of $W(x)$ (right) for $N = 24$ incidences and a $\lambda = 0.8$ wavelength when the crack is Γ_a.

where

$$\sigma_1 = \left\{(s, -0.5(s-0.2)^2 + 0.5) : s \in (-0.7, 0.3)\right\},$$
$$\sigma_2 = \left\{(s, (s-0.2)^3 + (s-0.2)^2) - 0.4 : s \in (-0.3, 0.7)\right\},$$

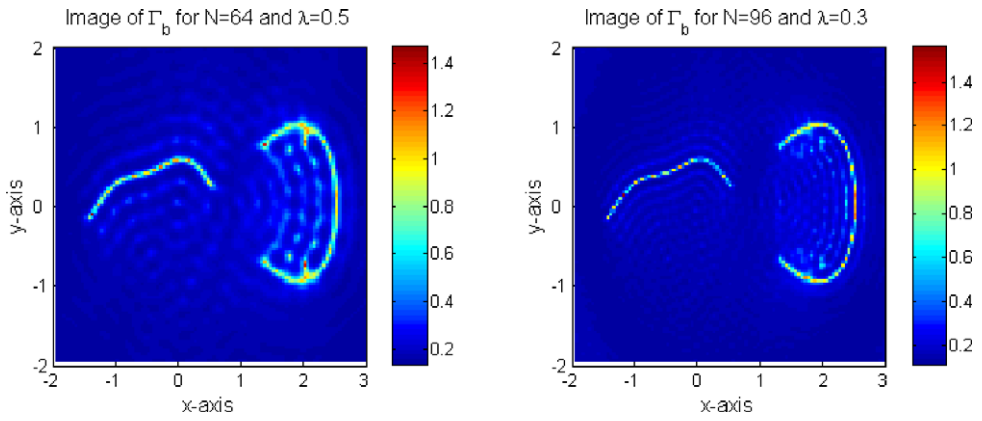

Fig. 13. (Dirichlet boundary condition) Maps of $W(x)$ for $N = 64$ incidences and a 0.5 wavelength (left), for $N = 96$ incidences and a 0.3 wavelength (right) when the crack is Γ_b.

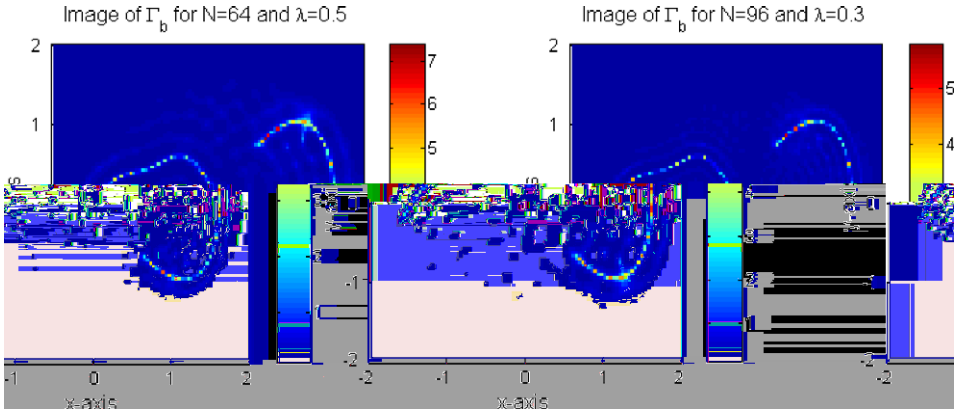

Fig. 14. (Dirichlet boundary condition) Same as Fig. 13 with 0.01 threshold.

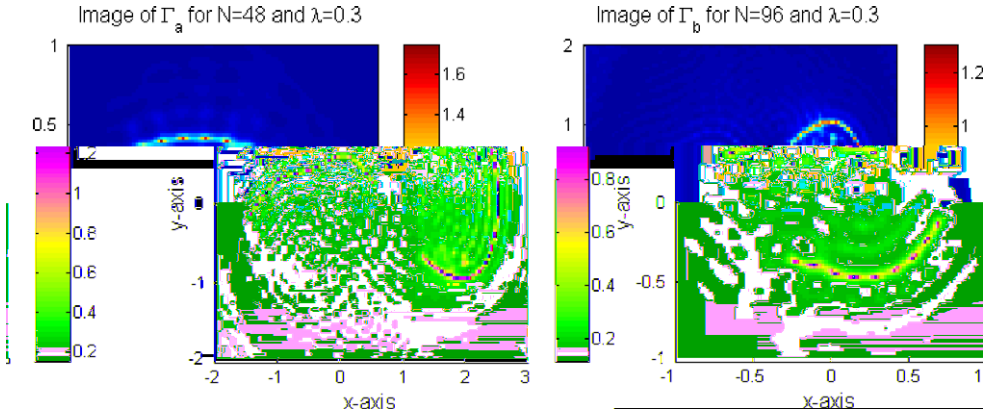

Fig. 15. (Dirichlet boundary condition) Maps of $W(x)$ for $N = 48$ incidences and a 0.3 wavelength when the crack is Γ_a (left) and for $N = 96$ incidences and a 0.3 wavelength when the crack is Γ_b (right). Dataset generated by the method introduced in [21] (compare to Figs. 11 and 13).

$$\sigma_3 = \left\{ \left(s - 0.5, \frac{1}{2}\cos\frac{s\pi}{2} + \frac{1}{5}\sin\frac{s\pi}{2} - \frac{1}{10}\cos\frac{3s\pi}{2} \right) : s \in [-1, 1] \right\},$$

$$\sigma_4 = \left\{ \left(2\sin\frac{s}{2} + 0.5, \sin s \right) : s \in \left[\frac{\pi}{4}, \frac{7\pi}{4} \right] \right\}.$$

Let us image Γ_a, K being collected for $N = 28$ and $N = 48$, and the wavelengths of operation $\lambda = 0.5$ and $\lambda = 0.3$, respectively. Corresponding images are displayed in Fig. 11. The discrimination is still obvious and images are as hoped for.

Remark 4.3. When we choose as the number of incident directions, $N = 24$, and as wavelength $\lambda = 0.8$, some isolated peaks of large magnitude appear between two cracks. In the several examples in the single-crack case, some disappear when we adopt a large number of illuminations or a 0.1 (or 0.01) threshold but via the previous methods, the one in Fig. 12 does not. To eliminate it, we must operate at a much smaller wavelength. In this example, this peak still shows up when the wavelength is larger than 0.6 and disappears when it becomes smaller than about 0.5, i.e., we now obtain proper images, refer to Fig. 11.

When the shape of cracks is getting complex, the discrimination is still obvious but unexpected isolated peaks appear. As an example, let us image Γ_b (refer to Fig. 13) at $\lambda = 0.5$ and $\lambda = 0.3$.

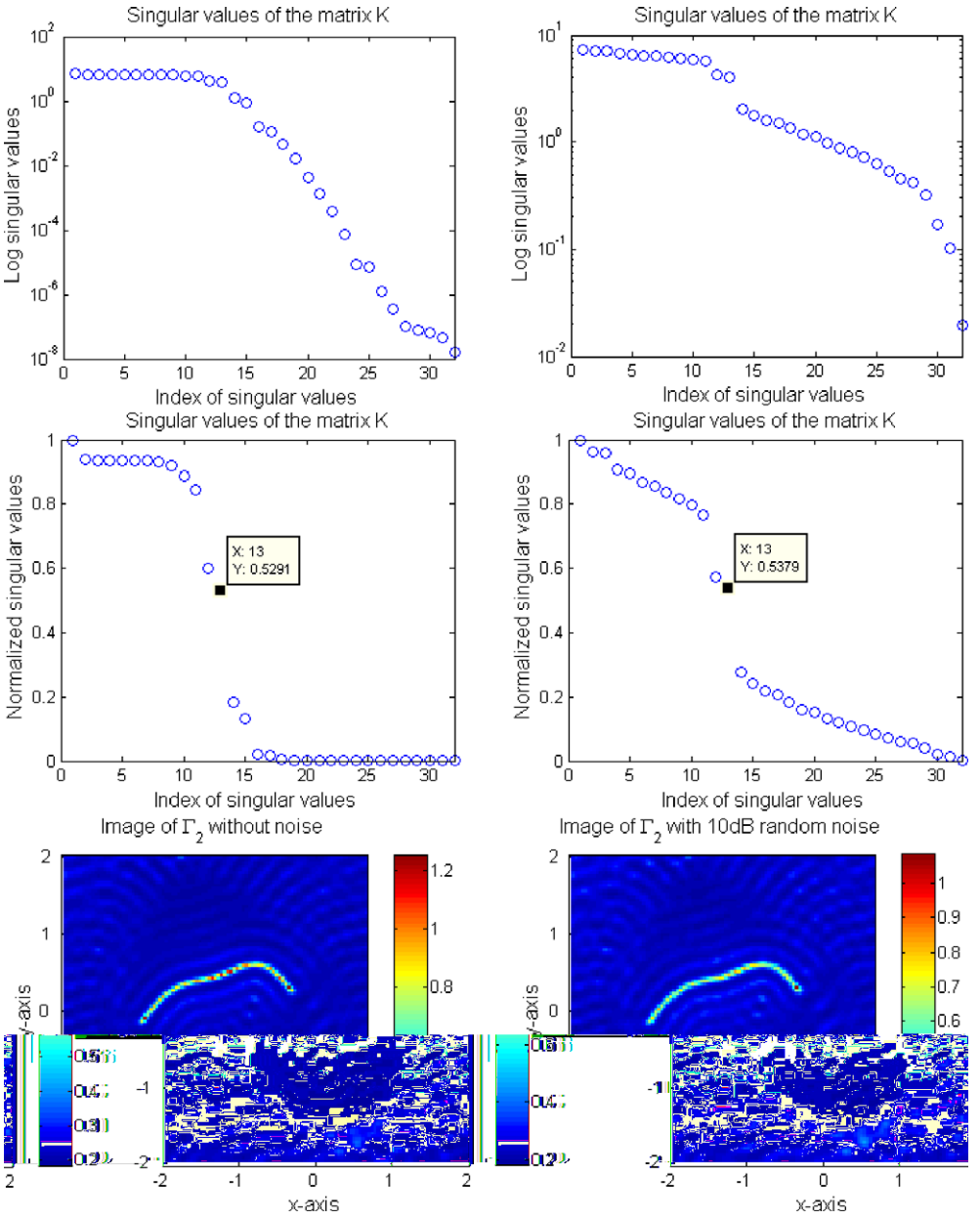

Fig. 16. (Dirichlet boundary condition) The distribution of log-scaled (top row) and normalized (center row) singular values of the matrix K and maps of $W(x)$ (bottom row) without noise (left column) and 10 dB random noise (right column) for all points $x \in \Omega$ for $N = 32$ incidences and a 0.4 wave length when the crack is Γ_2.

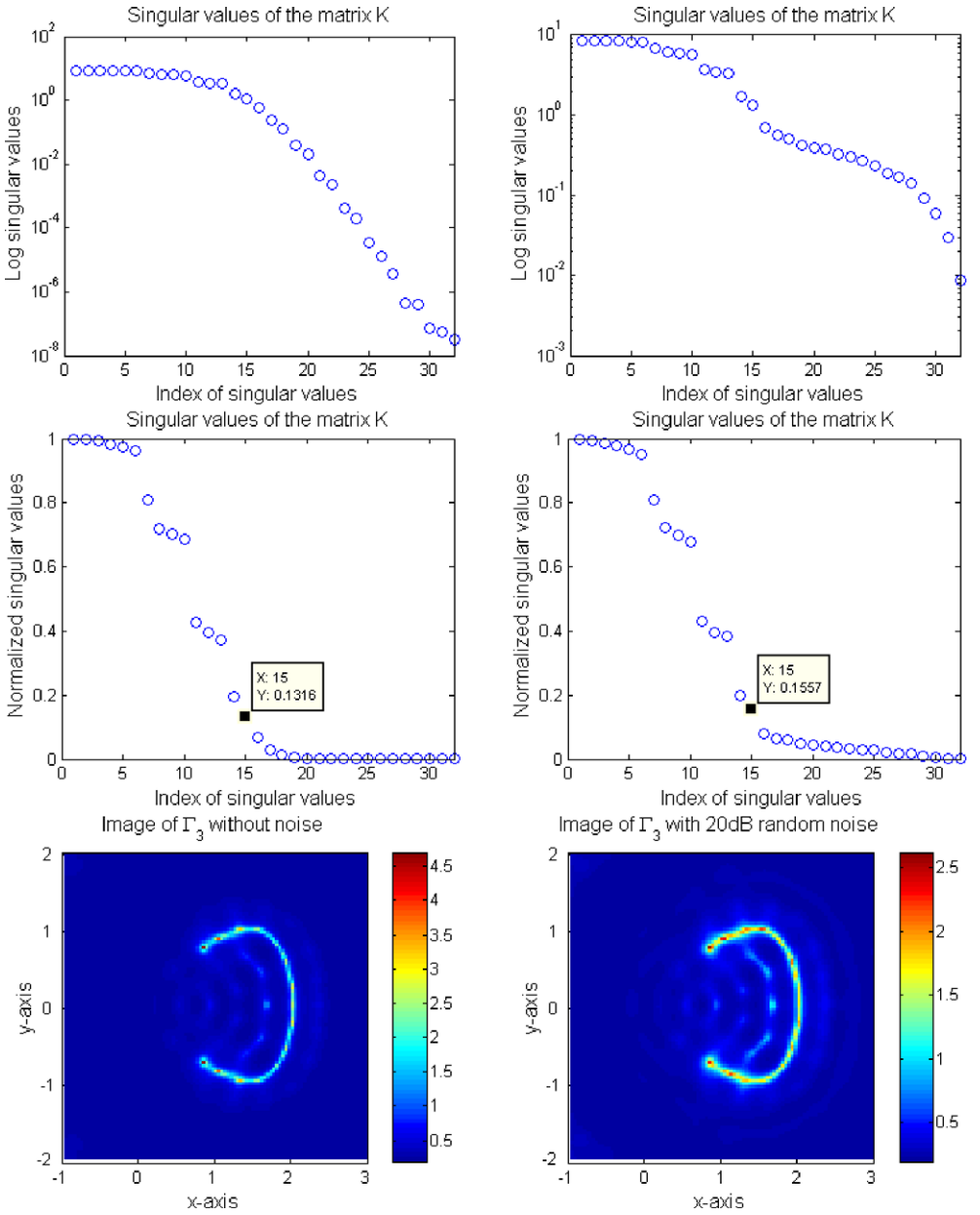

Fig. 17. (Dirichlet boundary condition) The distribution of log-scaled (top row) and normalized (center row) singular values of the matrix K and maps of $W(x)$ (bottom row) without noise (left column) and 20 dB random noise (right column) for all points $x \in \Omega$ for $N = 32$ incidences and a 0.7 wave length when the crack is Γ_3.

Similarly with the imaging of Γ_3 (see Fig. 7), we can eliminate these isolated peaks, i.e., proper images can be obtained, by adopting a 0.1 or 0.01 threshold (see Fig. 14).

We bring an end to this part with the following remark.

Remark 4.4. Similarly with the single-crack case, we can produce images from far-field data computed by the solution algorithm in [21, Chapter 4], refer to Fig. 15. By comparing the bottom row of Fig. 11 and top row of Fig. 15, and the bottom row of Fig. 13 and the same row of Fig. 15, such images look much like those from data acquired by the Nyström method.

4.3. Robustness with respect to noise

Let us assume that the collected far-field data is perturbed by a white Gaussian random noise added to the unperturbed data. If the signal-to-noise ratio of the data is large enough, one is able by SVD to extract proper information or the principal

components from the data, refer to, e.g., [14, Section 3.6]. Hence, if we successfully discriminate the signal subspace, the proposed algorithm will be quite robust with respect to noise.

In order to illustrate the robustness of the algorithm, let us image Γ_2 with 10 dB random noise. Typical results are in Fig. 16 at $\lambda = 0.4$. Although the distribution of log-scaled singular values is significantly different and some blurring appears

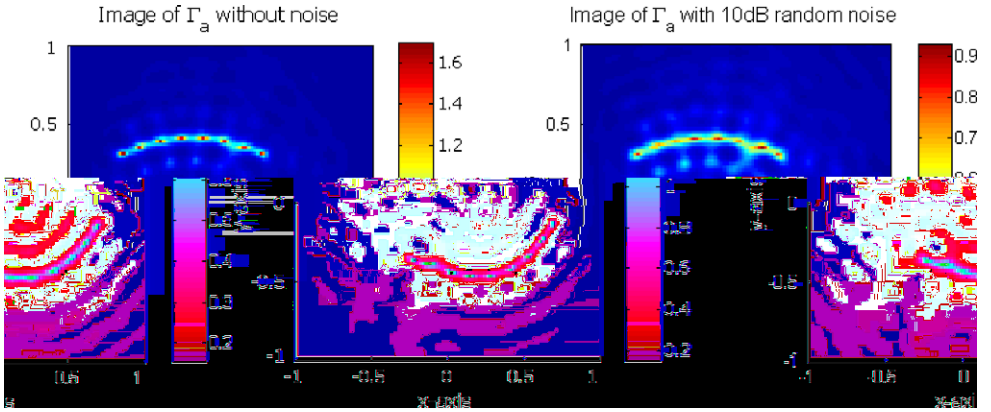

Fig. 18. (Dirichlet boundary condition) Maps of $W(x)$ without noise (left) and 10 dB random noise (right) for $N = 48$ incidences and a 0.3 wave length when the crack is Γ_a.

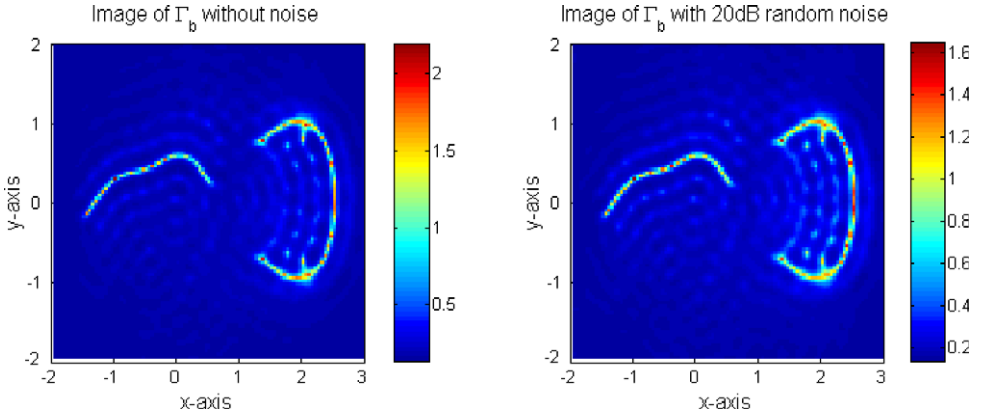

Fig. 19. (Dirichlet boundary condition) Maps of $W(x)$ without noise (left) and 20 dB random noise (right) for $N = 64$ incidences and a 0.5 wave length when the crack is Γ_b.

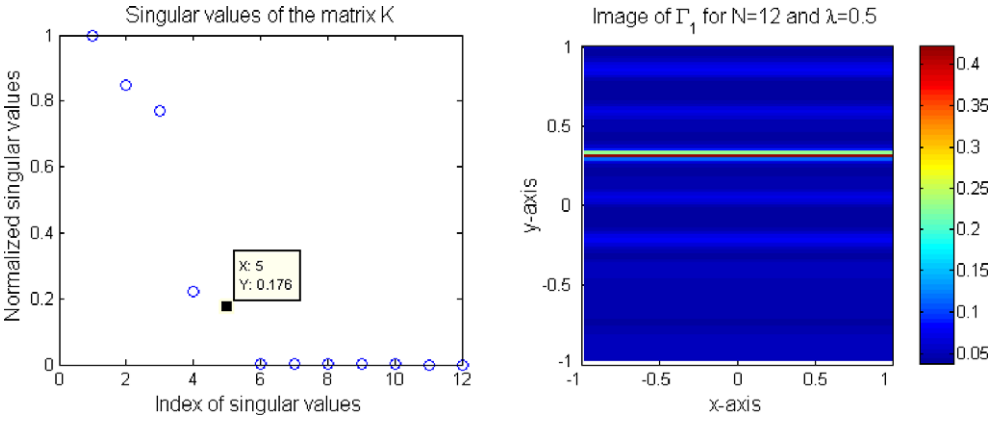

Fig. 20. (Neumann boundary condition) Distribution of normalized singular values of the matrix K (left) and map of $W(x)$ (right), for $N = 12$ incidences and a 0.5 wavelength when the crack is Γ_1.

in the image, we easily find proper singular values and obtain an accurate image via the normalizing method. For the case of Γ_3 with 20 dB random noise, a similar phenomenon occurs, refer to Fig. 17.

Fig. 21. (Neumann boundary condition) Maps of $W(x)$ for $N = 16$ incidences and a 0.5 wavelength (left) and for $N = 32$ incidences and a 0.2 wavelength (right) when the crack is Γ_1.

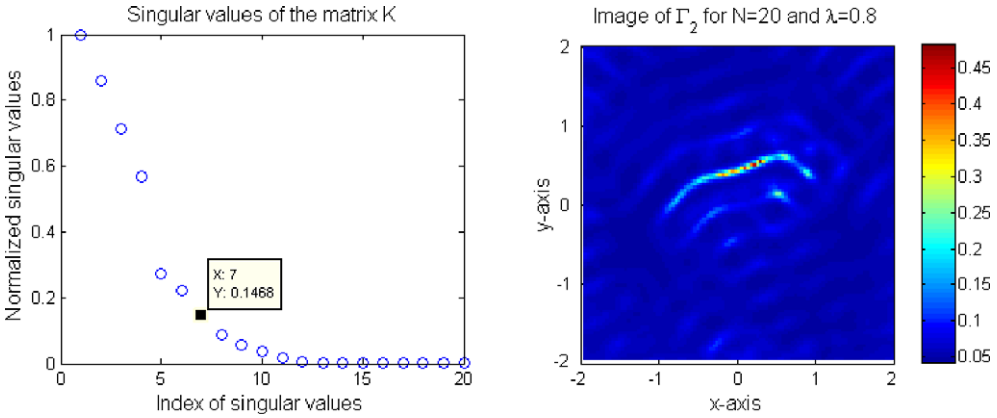

Fig. 22. (Neumann boundary condition) Distribution of normalized singular values of the matrix K (left) and map of $W(x)$ (right), for $N = 20$ incidences and a 0.8 wavelength when the crack is Γ_2.

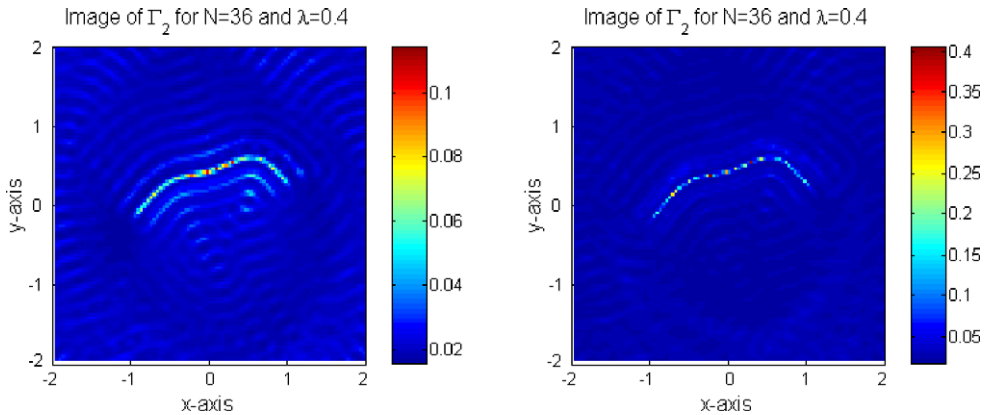

Fig. 23. (Neumann boundary condition) Maps of $W(x)$ for $N = 36$ incidences and a 0.4 wavelength when the crack is Γ_2. 0.1 (left) and 0.01 (right) threshold used for imaging.

This is verified as well for the multiple crack case. Typical images of Γ_a with 10 dB and Γ_b with 20 dB random noise are shown in Figs. 18 and 19, respectively.

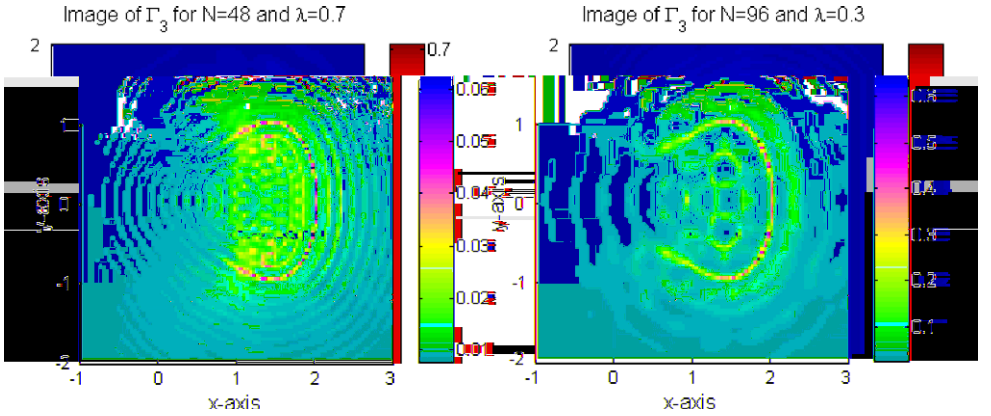

Fig. 24. (Neumann boundary condition) Maps of $W(x)$ for $N = 48$ incidences and a 0.7 wavelength (left) and for $N = 96$ and a 0.3 wavelength (right) when the crack is Γ_3. 0.01 threshold used for imaging.

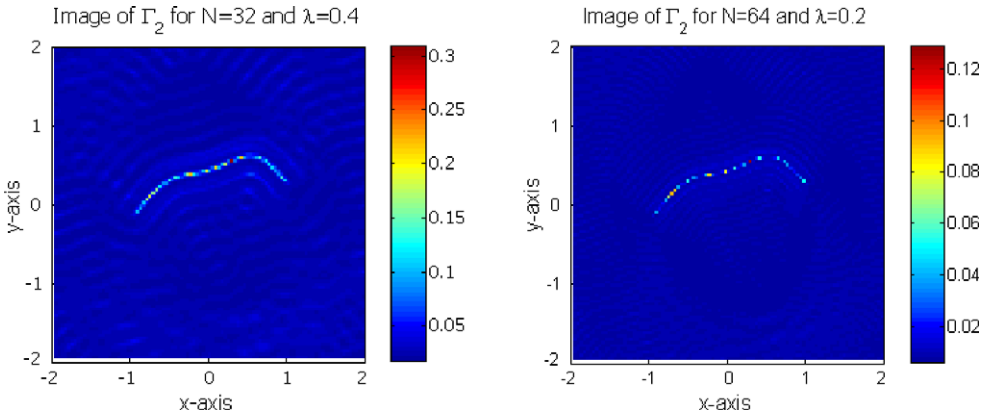

Fig. 25. (Neumann boundary condition) Maps of $W(x)$ for $N = 32$ incidences and a $\lambda = 0.4$ wavelength (left) and for $N = 64$ incidences and a $\lambda = 0.2$ wavelength (right) when the crack is Γ_2. Dataset generated by the solution algorithm introduced in [21] (compare to Fig. 23).

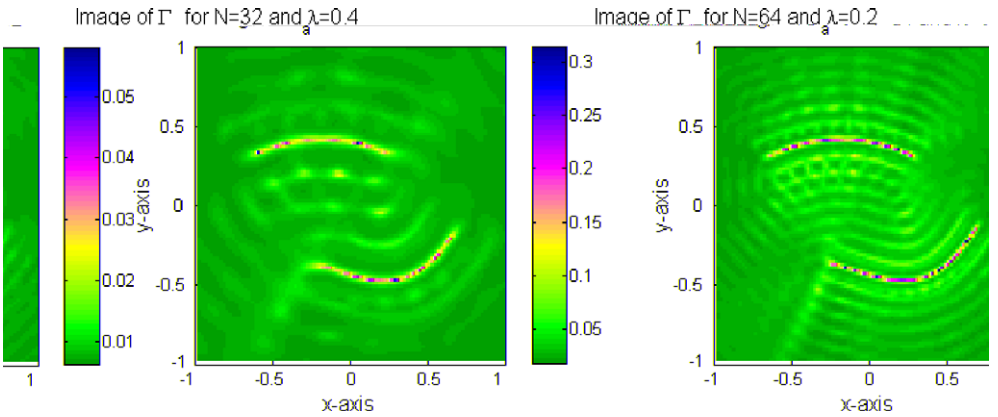

Fig. 26. (Neumann boundary condition) Maps of $W(x)$ for $N = 32$ incidences and a 0.4 wavelength (left) and for $N = 64$ incidences and a 0.2 wavelength (right) when the crack is Γ_a.

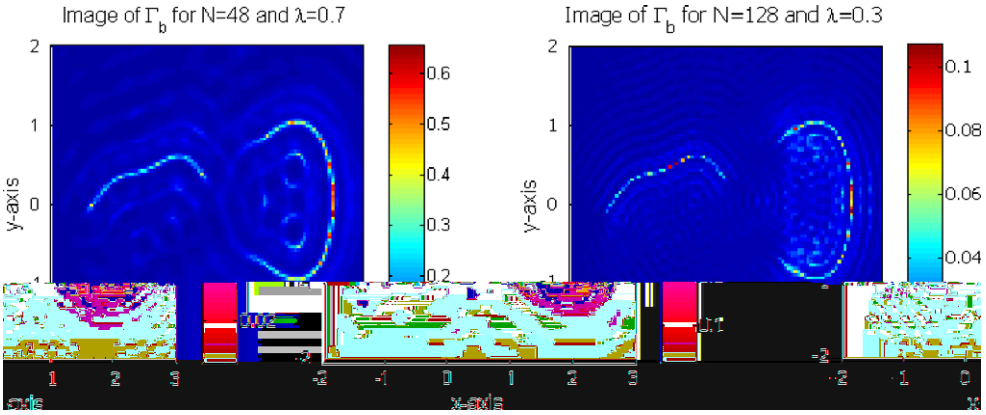

Fig. 27. (Neumann boundary condition) Maps of $W(x)$ for $N = 48$ incidences and a 0.7 wavelength (left) with $L = 64$ normal directions and for $N = 128$ incidences and a 0.3 wavelength (right) with $L = 128$ normal directions when the crack is Γ_b.

5. Numerical examples: Neumann boundary condition – TE

In this section, we present some imaging results for the Neumann boundary condition. The configuration is the same as previously and we use a set of fixed directions v_l as

$$v_l = \left(\cos\frac{2\pi l}{L}, \sin\frac{2\pi l}{L}\right) \quad \text{for } l = 1, 2, \ldots, L.$$

Throughout this section, we use $L = 16$ and 32 directions for the imaging of Γ_1 and Γ_2 and of Γ_3, respectively. Let us emphasize here that the fact that the direction normal to Γ is not known of us results in the slowness of the imaging, i.e., large computational costs are needed (about 3 minutes are required to obtain the top row result of Fig. 21 and 30 to obtain the one of Fig. 27 on a personal computer with 1.73 GHz dual-core pentium processor).

Now, we start up this section with the following remark.

Remark 5.1. Similarly with the Dirichlet boundary condition case, refer to Remark 4.1, when N is not large enough, the image is coarse. For example, when we choose $N = 12$ and as wavelength $\lambda = 0.5$, we observe that the first five normalized singular values are well distinguished from the seven next. However, when we use five singular values to discriminate the noise subspace from the signal subspace, poor results appear. Increasing N to 16 while keeping the same 0.5 wavelength (see Fig. 20), this phenomenon is vanishing, refer to Fig. 21.

For imaging Γ_1, K is collected for $N = 16$ and $N = 32$, and wavelengths $\lambda = 0.5$ and $\lambda = 0.2$, respectively. Maps of $W(x)$ are displayed in Fig. 21.

In contrast with the Dirichlet boundary condition case, see Fig. 5, when the crack is not anymore a straight line, a blurred image appears, refer to Fig. 22. In order to improve it, we can use a larger wavelength and a 0.01 threshold. This can be verified in Fig. 23.

Let us consider the imaging of Γ_3. Typical results are in Fig. 24 at $\lambda = 0.7$ and $\lambda = 0.3$. Let us notice that similarly with the previous result, the imaging is rather coarse for the 0.1 threshold, better for the 0.01 threshold.

Remark 5.2. Similarly with the Dirichlet boundary condition case, we can generate images from far-field data computed by the algorithm presented in [21, Chapter 3], refer to Fig. 25. By comparing to Fig. 23, such images look much like those built up from data computed by the Nyström method.

Let us apply the algorithm to the imaging of two inclusions (skipping all mathematical details), once emphasized that the dataset K is generated by solving the linear systems introduced in [21, Chapter 4]. A 0.01 threshold is adopted for higher resolution. We use $L = 32$ directions for imaging Γ_a and $L = 64$ and 128 directions for Γ_b, respectively.

Results for Γ_a are in Fig. 26, K being collected for $N = 32$ and $N = 64$, and for wavelengths $\lambda = 0.4$ and $\lambda = 0.2$, respectively. The few copies of the crack which show up in the maps are of much lower amplitude than the true one. From the images of Γ_b, refer to Fig. 27, we can verify this.

6. Conclusion

In this paper, we have proposed a non-iterative imaging algorithm for impenetrable, arc-like cracks modeled via a Dirichlet or Neumann boundary condition (TM and TE polarization in two-dimensional electromagnetics) which is based on a factorization of the MultiStatic Response matrix at a single frequency of operation and the use of a MUSIC cost functional.

Numerical experimentation from synthetic data computed by rigorous solution methods (like Nyström's) shows that this algorithm is fast, stable and overall quite effective, particularly in the TM (Dirichlet) case, at a lesser degree in the TE (Neumann) one, the case of limited views remaining to be appreciated carefully. The cracks are seen as a succession of peaks in a map, one each half-a-wavelength away from the next, enabling us to distinguish them from their embedding medium. Also, such a non-iterative imaging could fast provide initial guesses of a level-set evolution [1,13,24] or of a Newton-type algorithm [7,18,20].

For achieving the best imaging of a crack with Neumann boundary condition, the mathematical formulation for the choice of the normal direction on the crack still requires further investigation however.

References

[1] D. Àlvarez, O. Dorn, M. Moscoso, Reconstructing thin shapes from boundary electrical measurements with level sets, Int. J. Inf. Syst. Sci. 2 (2006) 498–511.
[2] H. Ammari, An introduction to mathematics of emerging biomedical imaging, Mathematics and Applications Series, vol. 62, Springer-Verlag, Berlin, 2008.
[3] H. Ammari, E. Bonnetier, Y. Capdeboscq, Enhanced resolution in structured media, submitted for publication.
[4] H. Ammari, E. Iakovleva, D. Lesselier, A MUSIC algorithm for locating small inclusions buried in a half-space from the scattering amplitude at a fixed frequency, Multiscale Model. Simulat. 3 (2005) 597–628.
[5] H. Ammari, E. Iakovleva, D. Lesselier, G. Perrusson, MUSIC-type electromagnetic imaging of a collection of small three-dimensional inclusions, SIAM J. Sci. Comput. 29 (2007) 674–709.
[6] H. Ammari, H. Kang, Reconstruction of Small Inhomogeneities from Boundary Measurements, Lecture Notes in Mathematics, vol. 184, Springer-Verlag, Berlin, 2004.
[7] H. Ammari, H. Kang, H. Lee, W.K. Park, Asymptotic imaging of perfectly conducting cracks, submitted for publication.
[8] F. Cakoni, D. Colton, The linear sampling method for cracks, Inverse Probl. 19 (2003) 279–295.
[9] F. Cakoni, D. Colton, E. Darrigrand, The inverse electromagnetic scattering problem for screens, Inverse Probl. 19 (2003) 627–642.
[10] M. Cheney, The linear sampling method and the MUSIC algorithm, Inverse Probl. 17 (2001) 591–595.
[11] D. Colton, H. Haddar, P. Monk, The linear sampling method for solving the electromagnetic inverse scattering problem, SIAM J. Sci. Comput. 24 (2002) 719–731.
[12] D. Colton, R. Kress, Inverse Acoustic and Electromagnetic Scattering Problems, Springer-Verlag, New York, 1998.
[13] O. Dorn, D. Lesselier, Level set methods for inverse scattering, Inverse Probl. 22 (2006) R67–R131.
[14] S. Hou, K. Solna, H. Zhao, A direct imaging algorithm for extended targets, Inverse Probl. 22 (2006) 1151–1178.
[15] S. Hou, K. Solna, H. Zhao, A direct imaging method using far-field data, Inverse Probl. 23 (2007) 1533–1546.
[16] A. Kirsch, The MUSIC-algorithm and the factorization method in inverse scattering theory for inhomogeneous media, Inverse Probl. 18 (2002) 1025–1240.
[17] A. Kirsch, S. Ritter, A linear sampling method for inverse scattering from an open arc, Inverse Probl. 16 (2000) 89–105.
[18] R. Kress, Inverse scattering from an open arc, Math. Meth. Appl. Sci. 18 (1995) 267–293.
[19] L. Mönch, On the numerical solution of the direct scattering problem for an open sound-hard arc, Computat. Appl. Math. 17 (1996) 343–356.
[20] L. Mönch, On the inverse acoustic scattering problem by an open arc: the sound-hard case, Inverse Probl. 13 (1997) 1379–1392.
[21] Z.T. Nazarchuk, Singular Integral equations in Diffraction Theory, vol. 210, Karpenko Physicomechanical Institute, Ukrainian Academy of Sciences, Lviv, 1994.
[22] W.K. Park, Inverse Scattering from Two-Dimensional Thin Inclusions and Cracks, Thèse de doctorat, Ecole Polytechnique, Feb. 2009, <http://paristech.bib.rilk.com/4834/>.
[23] W.K. Park, D. Lesselier, MUSIC-type imaging of a thin penetrable inclusion from its far-field multi-static response matrix, Inverse Probl. 25 (2009) 075002.
[24] W.K. Park, D. Lesselier, Reconstruction of thin electromagnetic inclusions by a level set method, Inverse Probl. 25 (2009) 085010.
[25] W.K. Park, D. Lesselier, On the imaging of scattering screens via fast solution methods, in: Proc. Int. Conf. Electromagn. Advanced Appl., ICEAA'09, Torino, Sept. 2009, in press.